JTTEE5 20:590–607
DOI: 10.1007/s11666-010-9604-y
1059-9630/$19.00 © ASM International

Multiobjective Optimization of Atmospheric Plasma Spray Process Parameters to Deposit Yttria-Stabilized Zirconia Coatings Using Response Surface Methodology

C.S. Ramachandran, V. Balasubramanian, and P.V. Ananthapadmanabhan

(Submitted July 5, 2010; in revised form September 29, 2010)

Atmospheric plasma spraying is used extensively to make Thermal Barrier Coatings of 7-8% yttria-stabilized zirconia powders. The main problem faced in the manufacture of yttria-stabilized zirconia coatings by the atmospheric plasma spraying process is the selection of the optimum combination of input variables for achieving the required qualities of coating. This problem can be solved by the development of empirical relationships between the process parameters (input power, primary gas flow rate, stand-off distance, powder feed rate, and carrier gas flow rate) and the coating quality characteristics (deposition efficiency, tensile bond strength, lap shear bond strength, porosity, and hardness) through effective and strategic planning and the execution of experiments by response surface methodology. This article highlights the use of response surface methodology by designing a five-factor five-level central composite rotatable design matrix with full replication for planning, conduction, execution, and development of empirical relationships. Further, response surface methodology was used for the selection of optimum process parameters to achieve desired quality of yttria-stabilized zirconia coating deposits.

Keywords atmospheric plasma spraying, optimization, response surface methodology, thermal barrier coatings, yttria-stabilized zirconia

1. Introduction

Plasma-sprayed yttria-stabilized zirconia (YSZ) coatings are being increasingly used as thermal barrier coatings (TBCs) for gas turbines and diesel engines (Ref 1). Effective TBCs should exhibit low thermal diffusivity, strong adherence to the substrate, phase stability, and thermal shock resistance during thermal cycling, and provide oxidation and corrosion protection to both the metallic bond coat and the substrate. Many studies have contributed to a better understanding of the metallographic preparation, microstructure, thermal conductivity and diffusivity, residual stresses, and failure mechanisms of the YSZ coatings (Ref 2-6). The impacts of the plasma spray process parameters on the coating characteristics and properties have generally been studied by means of classical one-factor-at-a-time or empirical approaches.

Plasma spraying, however, involves many parameters and complex interactions among them. The one-factor-at-a-time approach requires prohibitively large numbers of trials to systematically identify the effects of the process parameters, and therefore the effects of the process parameters on the microstructure and properties of the YSZ coatings have not been fully understood yet. Statistical designs of experiments have been shown to provide efficient approaches to systematically investigate the process parameters of thermal spray. The Taguchi method was efficiently used by Kingswell et al. (Ref 7) to investigate the vacuum plasma spray deposition of alumina, nickel-based alloys, and tungsten carbide/cobalt cermet coatings. The small central composite design method was employed by Wang and Coyle (Ref 8) to optimize solution precursor plasma spray process parameters to deposit NiYSZ coatings on SOFCs. Statistical design of experiment by the response surface methodology (RSM) was used to successfully optimize the microhardness of plasma-sprayed WC-12%Co (Ref 9).

For satisfactory functioning of the sprayed TBC material, it is essential to maintain adequate bond strength between the coatings and the substrate. Tensile bond strength, porosity, and microhardness are the basic and key quality characteristics to understand the microstructure and properties of thermal spray coatings (Ref 10). Deposition efficiency in atmospheric plasma spray (APS) system is regarded as being closely related

C.S. Ramachandran and **V. Balasubramanian**, Department of Manufacturing Engineering, Annamalai University, Annamalai Nagar 608 002, Tamilnadu, India; and **P.V. Ananthapadmanabhan**, Plasma Spray Technologies Section (PSTS), Laser and Plasma Technology Division (L&PTD), Bhabha Atomic Research Centre (BARC), Anu Shakthi Nagar, Trombay, Mumbai 400 085, Maharashtra, India. Contact e-mail: csrcn@rediffmail.com.

to the melting state of feedstock material (Ref 11). High deposition efficiency is very important to lower the cost and shorten the process time, especially for spraying thick and large-scale coatings (Ref 12). Porous YSZ coatings are useful to lower thermal conductivity (Ref 13). Dense YSZ coatings with high microhardness, in some cases, are expected to improve the erosion and corrosion resistance as well as the oxidation resistance of the metallic bond coating (Ref 14). YSZ is perhaps the most-studied thermal spray material, and thus there is a lot of precedent for this study. Studies have been carried out using advanced on-line particle-monitoring systems to measure the temperature and velocity of in-flight particles and to correlate them with the deposition efficiency, porosity, and other microstructure features of YSZ coatings (Ref 15-18).

However, optimization of plasma spray process involving multiple factors and multiple responses has hardly been reported in the literature. Hence, this article deals with the application of RSM in developing empirical relationships relating important input variables, namely, the power (P), the primary gas flow rate (G), the stand-off distance (S), the powder feed rate (F), and the carrier gas flow rate (C), to the deposition efficiency, the tensile bond strength, the lap shear bond strength, the porosity, and the hardness of the APS-YSZ TBCs. Further, this article illustrates how a number of overlapping response surfaces can be used to select the operating conditions necessary to achieve the desired specifications and for the optimization of the plasma spraying process. It should be emphasized that the range selected for parameters, the results, and the conclusions refer specifically to the torch, the chemical composition, and the morphology of the powder material used in this study. However, the illustrated approach and the methodology of the response surfaces are universal.

2. Scheme of Investigation

In order to achieve the desired objective, the present investigation was planned in the following sequence:

1. To identify the important APS process parameters;
2. To find the upper and lower limits of the identified parameters;
3. To choose the relevant experimental design matrix;
4. To conduct the experiments as per the design matrix;
5. To record the responses (measuring the tensile bond strength, lap shear bond strength, hardness, porosity, and deposition efficiency);
6. To formulate empirical relationships to predict the aforementioned responses using RSM;
7. To perform numerical and graphical optimization;
8. To conduct confirmatory test using optimized process parameters;
9. To conclude with results and discussions.

2.1 Identifying the Important Process Parameters

From the literature (Ref 19-21) and the previous study done in our laboratory, the predominant factors (APS process parameters) that have a greater influence on the coating properties were identified. They are (i) the power (kW), (ii) the primary gas flow rate (lpm), (iii) the stand-off distance (mm), (iv) the powder feed rate (gpm), and (v) the carrier gas flow rate (lpm).

2.2 Finding the Working Limits of the Parameters

A large number of spray trial runs were carried out on grit blasted 3-mm-thick AISI 316 austenitic stainless steel plates to determine the feasible working limits of APS parameters. Plasma spray deposition was carried out using an APS system 40 kW IGBT-based Plasmatron (Make: Ion Arc Technologies; India. Model: APSS-II). The feed stock was H.C. Stark, AMPERIT 827.054 powder (ZrO_2, 7% Y_2O_3) with particle size of $45 + 10$ μm. The YSZ powder was directly sprayed on to the grit-blasted substrate and bond coat was not used. Different combinations of APS process parameters were used to carry out the trial runs. Coating thickness for all the deposits was maintained at 300 ± 15 μm. To fix the limits of the considered factors, a couple of criteria were adopted. The criteria were that the coatings must have minimum tensile bond strength of 3 MPa and they must be deposited with a minimum deposition efficiency of 30%. During the trials, the following observations were made.

(i) If the spray was carried out below 22 kW power level, then poor adhesion and subsequent delamination of the coating were observed. If the power level was increased beyond 30 kW, then the surface evaporation from particles leading to vapor entrapment in the deposit and poor deposition efficiency were observed. (ii) If the primary gas flow rate was below 25 lpm, then anode erosion was observed, and if it was above 45 lpm, then arc blow out was observed. (iii) If the stand-off distance was less than 90 mm, then distortion of the substrate and peeling off of the coating were observed, and if it was increased beyond 130 mm, then re-solidification of the molten particles resulting in poor coating adhesion and poor deposition efficiency was observed. (iv) The minimum possible powder feed rate was 15 gpm (limitation of the powder feeding system). If the powder feed rate was increased beyond 35 gpm, then a large fraction of the powder particles remain in the nonmolten condition, consequently, resulting in low spray deposition efficiency and coating delamination. (v) If the carrier gas flow rate was below 3 lpm, then the powder could not penetrate the plasma, and if it was increased beyond 11 lpm, then the powder passed right across the plasma column resulting in the erosion of anode (nozzle) edges. Nitrogen was used as secondary gas, and its flow rate was kept constant at 4 lpm.

2.3 Choosing the Experimental Design Matrix

After considering all of the aforementioned conditions, the feasible limits of the parameters were chosen so that reasonably good adherent coatings could be obtained.

A central composite rotatable design of second order was found to be the most efficient tool in RSM to establish the empirical relationship of the response surfaces using the smallest possible number of experiments without a loss of accuracy (Ref 22). Owing to a wide range of factors, the use of five-factors and five-level central composite design matrix was chosen to optimize the experimental conditions.

With a view to achieving the aforementioned aim, statistically designed experiments based on a factorial technique were used to reduce the cost and time and to obtain the required information pertaining to the main and interaction effects on the response parameters. Table 1 presents the ranges of factors considered, and Table 2 shows the 32 sets of coded conditions used to form the design matrix. The first 16 experimental conditions are derived from a half-factorial experimental design matrix ($2^{5-1} = 16$). All of the variables at the intermediate (0) level constitute the centre points while the combinations of each process variable at either the lowest (−2) or the highest (+2) value with the other four variables of the intermediate levels constitute the star points. Thus, the 32 experimental runs allowed for the estimation of the linear, quadratic, and two-way interactive effects of the variables on the APS-YSZ coating deposits. The method of designing such a matrix is dealt with elsewhere (Ref 23, 24). For the convenience of recording and processing experimental data, the upper and lower levels of the factors are coded here as +2 and −2, respectively. The coded values of any intermediate value can be calculated using the following relationship:

Table 1 Considered factors and their levels

			Levels				
Factors	**Notations**	**Units**	**Lowest (−2)**	**Low (−1)**	**Middle (0)**	**High (+1)**	**Highest (+2)**
Power	*P*	kW	22	24	26	28	30
Primary gas flow rate	*G*	lpm	25	30	35	40	45
Stand-off distance	*S*	mm	90	100	110	120	130
Powder feed rate	*F*	gpm	15	20	25	30	35
Carrier gas flow rate	*C*	lpm	3	5	7	9	11

Table 2 Experimental design matrix

Spray condition	Input power	Primary gas flow rate	Stand-off distance	Powder feed rate	Carrier gas flow rate	Deposition efficiency, %	Adhesion strength, MPa	Shear strength, MPa	Porosity, vol.%	Hardness, HV 0.3
1	−1	−1	−1	−1	1	44	9	5	20	710
2	1	−1	−1	−1	−1	59	17	8	8	954
3	−1	1	−1	−1	−1	49	7	5	11	792
4	1	1	−1	−1	1	67	21	11	4	1082
5	−1	−1	1	−1	−1	42	5	2	25	675
6	1	−1	1	−1	1	39	7	3	22	683
7	−1	1	1	−1	1	47	10	5	23	757
8	1	1	1	−1	−1	60	14	6	11	966
9	−1	−1	−1	1	−1	42	4	3	25	675
10	1	−1	−1	1	1	58	13	5	14	943
11	−1	1	−1	1	1	47	9	5	19	757
12	1	1	−1	1	−1	63	16	7	9	1024
13	−1	−1	1	1	1	32	4	2	25	512
14	1	−1	1	1	−1	40	5	3	24	652
15	−1	1	1	1	−1	41	6	2	25	663
16	1	1	1	1	1	45	8	7	17	733
17	−2	0	0	0	0	41	6	3	23	663
18	2	0	0	0	0	64	19	9	6	1036
19	0	−2	0	0	0	38	8	3	23	617
20	0	2	0	0	0	53	15	8	11	861
21	0	0	−2	0	0	66	16	7	7	1071
22	0	0	2	0	0	48	7	2	23	780
23	0	0	0	−2	0	58	18	8	12	943
24	0	0	0	2	0	48	13	5	21	780
25	0	0	0	0	−2	58	10	6	13	943
26	0	0	0	0	2	53	11	9	14	861
27	0	0	0	0	0	70	23	11	5	1129
28	0	0	0	0	0	72	22	12	4	1164
29	0	0	0	0	0	70	23	11	5	1129
30	0	0	0	0	0	71	22	12	4	1140
31	0	0	0	0	0	70	23	11	5	1129
32	0	0	0	0	0	72	22	12	4	1164

$$X_i = 2[2X - (X_{max} + X_{min})]/(X_{max} - X_{min}) \quad \text{(Eq 1)}$$

where X_i is the required coded value of a variable X, X is any value of the variable from X_{min} to X_{max}, X_{min} is the lower level of the variable, and X_{max} is the highest level of the variable.

2.4 Conducting the Experiments

In this investigation, 32 coating deposits were prepared using different combinations of APS process parameters, as prescribed by the experimental design matrix (Table 2). The experiments were conducted in a random order to prevent systematic errors from infiltrating the system. To evaluate the coating properties, four geometries of coated substrates were used: (i) 25.4 mm × 25.4 mm (diameter × height) cylindrical specimens for tensile bond strength test, (ii) 25.4 × 50.8 × 3 mm coupons for lap shear bond strength test, (iii) 25.4 × 25.4 mm coupons for metallographic examination and hardness measurement, and (iv) 50.8 × 50.8 × 3 mm coupons for deposition efficiency measurement. The substrates were prepared by grit blasting before the deposition of the coating. Grit blasting was carried out using corundum grits of size of 500 + 320 μm and subsequently cleaned using acetone in an ultrasonic bath and dried. After grit blasting, the average surface roughness was measured using the surface roughness tester. (Make: Mitutoyo, Japan; Model: Surftest 301) The average roughness was found to be 5 μm.

2.5 Recording the Responses

The tensile bond strength test was carried out as per ASTM C 633 (Fig. 1) standard, and the lap shear bond strength test was carried out as per EN 1465 (Fig. 2) standard using a universal testing machine (Make: FIE-Blue Star, India; Model: UNITEK-94100). From the

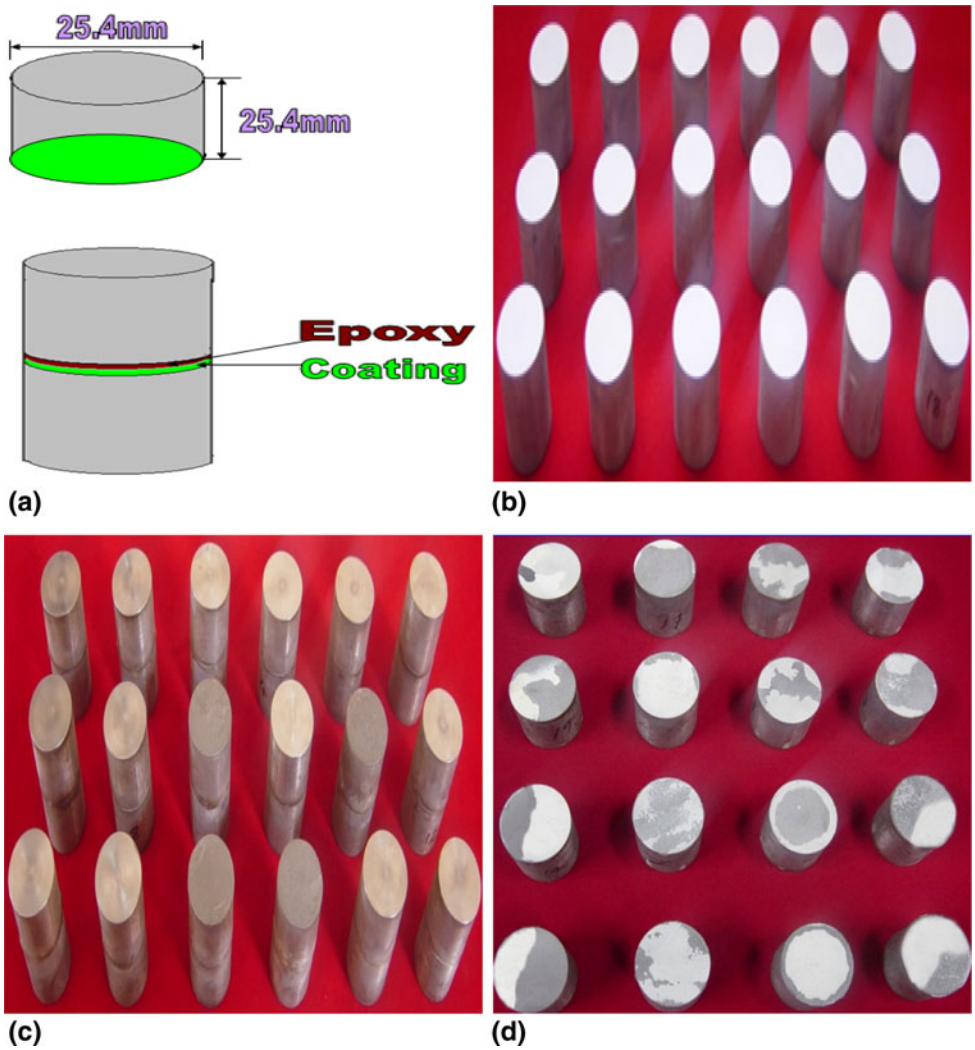

Fig. 1 Details of tensile bond strength test. (a) Dimensions of tensile bond strength test specimens (ASTM C 633). (b) Coated specimens for tensile bond strength test. (c) Epoxy bonded specimens for tensile bond strength test. (d) Specimens after tensile bond strength test

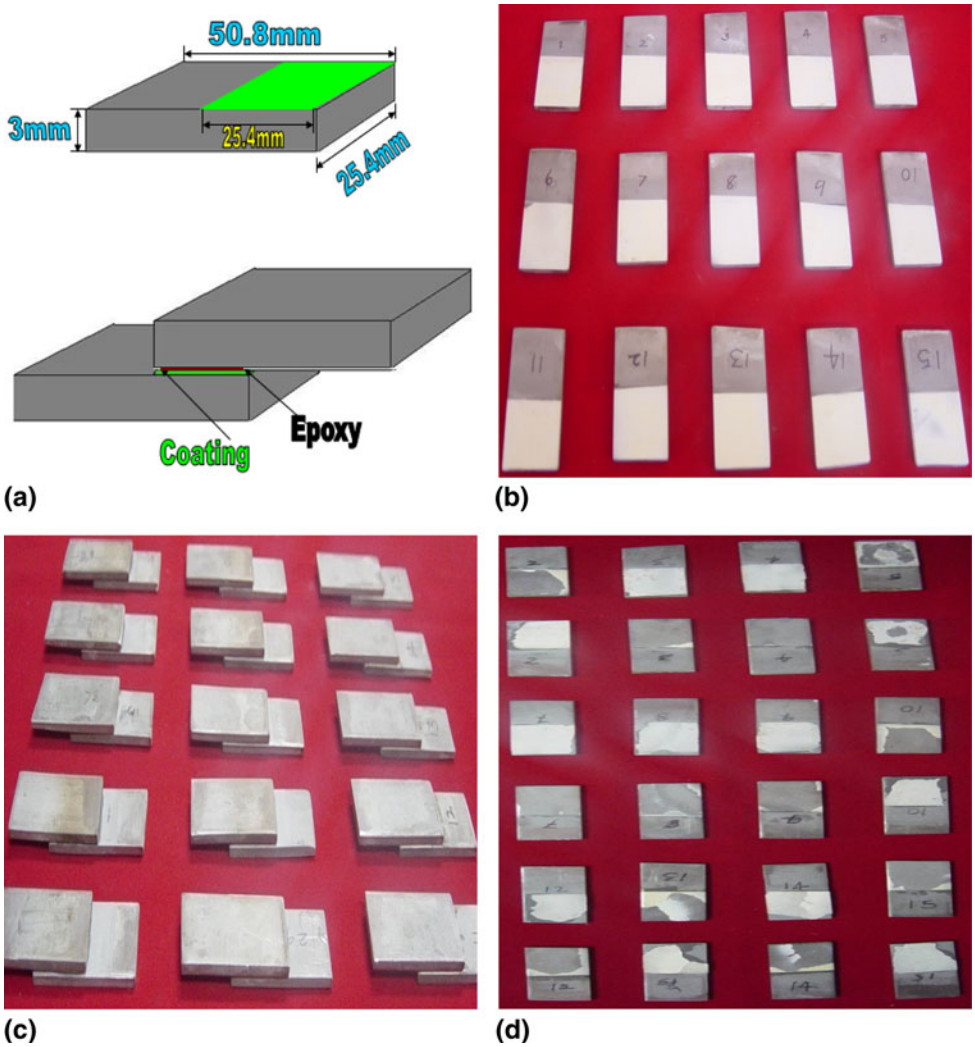

Fig. 2 Details of lap shear bond strength test. (a) Dimensions of lap shear bond strength test specimens (EN 1465). (b) Coated specimens for lap shear bond strength test. (c) Epoxy bonded specimens for lap shear bond strength test. (d) Specimens after lap shear bond strength test

Fig. 1(d) and 2(d), it could be inferred that a few of the bond test specimens present partial (combined adhesive and cohesive) coating failures. The basic bond strength may be evaluated by the degree of coverage of the remaining particles which remain bonded even after the testing of bonding strength (Ref 25). Hence, whenever a bond test presented a partial failure like those shown in Fig. 1(d) and 2(d), the true bond strength was evaluated from that coating area remaining on the substrate after the test, which was intact and did not detach or fail. For each experimental condition, three coated specimens were prepared and tested to minimize experimental errors.

A commercially available heat-curable epoxy was used as an adhesive to test the coated specimens. The tensile bond strength and lap shear bond strength values of the epoxy were found to be 65 and 34 MPa, respectively. The porosity was analyzed on the polished cross section of the coating using optical microscope (Make: MEIJI, Japan; Model: MIL-7100) equipped with image analyzing system. Standard metallographic procedures were adopted to polish the cross section of the coatings. A 200-μm square area was selected on the polished cross section of the coating, and the image was analyzed. The same procedure was repeated at five random locations to find out the average percentage volume of porosity. The Microhardness measurement was made using Vickers microhardness tester (Make: Shimadzu, Japan; Model: HMV-2T). 300 g load and 15-s dwell time were used to evaluate the hardness. Hardness values were measured at ten random locations on the polished cross section of the coating. The deposition efficiency was calculated from the coating mass and the corresponding feedstock mass that was delivered to the torch. The former was directly measured using a weighing balance with a resolution of 0.01 g. The latter was determined from the powder feed rate and the spraying time (30 s) on the substrate.

3. Predictive Model for Responses

In this study, a response surface model-building technique was utilized to predict tensile bond strength, lap shear bond strength, microhardness, porosity, and deposition efficiency in terms of various process parameters for APS process. Details of the model-building technique are discussed below.

3.1 Response Surface Methodology (RSM)

In practical applications of RSM, it is necessary to develop a fitting model for the response surface; this is typically driven by some unknown physical mechanism. For prediction, RSM is practical, economical, and relatively easy for use (Ref 26). The RSM consists of an experimental strategy that explores the space of the process-independent variables, empirical statistical modeling to develop an appropriate relationship between the yield and the process variables, and optimization methods to determine the levels or values of the process variables that produce desirable response values (Ref 27). In the present investigation, to correlate the process parameters and the responses of APS coating deposits, a second-order quadratic model was developed to predict the responses based on the experimentally measured values. The responses are a function of power (P), primary gas flow rate (G), stand-off distance (S), powder feed rate (F), and carrier gas flow rate (C), and it can be expressed as

$$\text{Responses} = f(P, G, S, F, C) \quad \text{(Eq 2)}$$

The model chosen includes the effects of the main and interaction effects of all factors. The model selected is polynomial, and is expressed as follows:

$$Y = b_0 + \sum b_i x_i + \sum b_{ii} x_i^2 + \sum b_{ij} x_i x_j \quad \text{(Eq 3)}$$

For the five factors, the selected polynomial can be expressed as

$$\begin{aligned} Y = {} & b_0 + b_1(P) + b_2(G) + b_3(S) + b_4(F) + b_5(C) \\ & + b_{11}(P^2) + b_{22}(G^2) + b_{33}(S^2) + b_{44}(F^2) \\ & + b_{55}(C^2) + b_{12}(PG) + b_{13}(PS) + b_{14}(PF) \\ & + b_{15}(PC) + b_{23}(GS) + b_{24}(GF) + b_{25}(GC) \\ & + b_{34}(SF) + b_{35}(SC) + b_{45}(FC) \end{aligned} \quad \text{(Eq 4)}$$

where b_0 is the average of responses, and b_1, b_2,..., b_{23} are the coefficients that depend on their respective main and interaction effects of the parameters. The values of the coefficients were calculated using the following expressions:

$$b_0 = 0.1591\left(\sum Y\right) - 0.0341 \sum\sum (X_{ii} Y) \quad \text{(Eq 5)}$$

$$b_i = 0.04167 \sum (X_i Y) \quad \text{(Eq 6)}$$

$$\begin{aligned} b_{ii} = {} & 0.03125 \sum (X_{ii} Y) + 0.00284 \sum\sum (X_{ii} Y) \\ & - 0.03409 \left(\sum Y\right) \end{aligned} \quad \text{(Eq 7)}$$

$$b_{ij} = 0.0625 \sum (X_{ij} Y) \quad \text{(Eq 8)}$$

To estimate the regression coefficients, a number of experimental design techniques are available. In this study, a five-factor, five-level central composite rotatable design was used. The regression coefficients were calculated with the help of Design Expert V 8.1 statistical software. After determining the coefficients (at a 95% confidence level), the final empirical relationships were developed using these coefficients. The final statistical model to estimate the responses are given below:

$$\begin{aligned} & \text{Deposition efficiency } (\%) \\ & = 70.78 + 5.54(P) + 3.875(G) - 4.96(S) - 2.46(F) \\ & \quad - 1.13(C) + 0.94(PG) - 2.69(PS) + 0.063(PF) \\ & \quad - 0.56(PC) + 1.06(GS) - 0.94(GF) + 0.19(GC) \\ & \quad - 1.31(SF) - 1.44(SC) + 0.56(FC) - 4.53P^2 \\ & \quad - 6.28G^2 - 3.41S^2 - 4.41F^2 - 3.78C^2 \end{aligned} \quad \text{(Eq 9)}$$

$$\begin{aligned} & \text{Tensile Bond Strength (MPa)} \\ & = 22.51 + 3.042(P) + 1.71(G) - 2.291(S) - 1.46(F) \\ & \quad + 0.38(C) + 0.44(PG) - 1.81(PS) - 0.56(PF) \\ & \quad - 0.81(PC) + 0.44(GS) - 0.063(GF) + 0.19(GC) \\ & \quad - 0.063(SF) - 0.56(SC) - 0.063(FC) - 2.51P^2 \\ & \quad - 2.76G^2 - 2.76S^2 - 1.76F^2 - 3.01C^2 \end{aligned} \quad \text{(Eq 10)}$$

$$\begin{aligned} & \text{Lap Shear Bond Strength (MPa)} \\ & = 11.44 + 1.38(P) + 1.13(G) - 1.21(S) - 0.71(F) \\ & \quad + 0.54(C) + 0.44(PG) - 0.31(PS) - 0.063(PF) \\ & \quad - 0.19(PC) + 0.19\,(GS) - 0.063(GF) + 0.56(GC) \\ & \quad + 0.44(SF) + 0.063(SC) + 0.063(FC) - 1.32P^2 \\ & \quad - 1.44G^2 - 1.69S^2 - 1.19F^2 - 0.94C^2 \end{aligned} \quad \text{(Eq 11)}$$

$$\begin{aligned} & \text{Porosity (vol.\%)} \\ & = 4.57 - 4.087(P) - 2.837(G) + 3.92(S) + 2.17(F) \\ & \quad + 0.33(C) - 0.63(PG) + 1(PS) + 0.25(PF) \\ & \quad + 0.25(PC) + 0.25(GS) + 0.5(GF) + 0.5(GC) \\ & \quad - 0.875(SF) - 0.125(SC) - 1.38(FC) + 2.43P^2 \\ & \quad + 3.06G^2 + 2.56S^2 + 2.93F^2 + 2.18C^2 \end{aligned} \quad \text{(Eq 12)}$$

$$\begin{aligned} & \text{Hardness (HV 0.3)} \\ & = 1142.07 + 93.42(P) + 60.75(G) - 78.25(S) \\ & \quad - 41.08(F) - 16.17(C) + 11(PG) - 40.13(PS) \\ & \quad - 0.38(PF) - 5.38(PC) + 14(GS) - 11.25(GF) \\ & \quad - 0.5(GC) - 23.88(SF) - 19.88(SC) + 5.38(FC) \\ & \quad - 72.82P^2 - 100.44G^2 - 53.82S^2 - 69.82F^2 - 59.69C^2 \end{aligned} \quad \text{(Eq 13)}$$

3.2 Checking the Adequacy of the Model

In this investigation, analysis of variance (ANOVA) is used to check the adequacy of the developed empirical relationships (Ref 28). ANOVA test results of the responses, namely, the tensile bond strength and porosity are presented in Table 3 and 4, respectively. The adequacy of the model was tested using the ANOVA technique. In this study, the model F value and the associated probability values are checked to confirm the significance of the empirical relationships. Further, using the *F*-values, the predominant factors which have the major and minor effects on the responses could be assessed. From the F value assessment, it was found that the predominant factors which have direct influence on the responses as per hierarchy are power, stand-off distance, primary gas flow rate, powder feed rate, and carrier gas flow rate. The determination coefficient (R^2) indicates the goodness of fit for the model. In all the cases, the value of the determination coefficient ($R^2 > 0.99$) indicates that less than 1% of the total variations are not explained by the empirical relationships. The value of the adjusted determination coefficient is also high, which indicates the high significance of the empirical relationships. The predicted R^2 values also show good agreement with the adjusted R^2 values. Adequate precision compares the range of the predicted values at the design points with the average prediction error. At the same time, a relatively low value of the coefficient of variation indicates the improved precision and the reliability of the conducted experiments. The value of probability $> F$ in Table 3 and 4 for the empirical relationships are less than 0.05, which indicates that the empirical relationships are significant. Lack of fit was not significant for all the developed empirical relationships as desired (Ref 29). The normal probability plots for the responses are shown in Fig. 3. From the figure, it could be inferred that the residuals fall on the straight line, which shows that the errors are distributed normally (Ref 30). Collectively, these results indicate the excellent capability of the regression model. Further, each observed value matches its experimental value well, as shown in Fig. 4.

4. Results and Discussion

The developed empirical relationships can be used effectively to predict the responses by substituting process parameter values in coded form. Based on these empirical relationships, the main and interaction effects of the process parameters on the coating properties were computed and plotted in form of perturbation plots, as shown in Fig. 5. The perturbation plot is an important diagrammatic

Table 3 ANOVA for the response tensile bond strength

Source	Sum of squares	df	Mean square	*F* value	*p* value Prob $> F$	
Model	1303.931	20	65.19654	257.2429	<0.0001	Significant
P, input power	222.0417	1	222.0417	876.0992	<0.0001	
G, primary gas flow rate	70.04167	1	70.04167	276.3601	<0.0001	
S, stand-off distance	126.0417	1	126.0417	497.3166	<0.0001	
F, powder feed rate	51.04167	1	51.04167	201.3927	<0.0001	
C, carrier gas flow rate	3.375	1	3.375	13.31658	0.0038	
PG	3.0625	1	3.0625	12.08356	0.0052	
PS	52.5625	1	52.5625	207.3933	<0.0001	
PF	5.0625	1	5.0625	19.97486	0.0009	
PC	10.5625	1	10.5625	41.67595	<0.0001	
GS	3.0625	1	3.0625	12.08356	0.0052	
GF	0.0625	1	0.0625	0.246603	0.6293	
GC	0.5625	1	0.5625	2.219429	0.1644	
SF	0.0625	1	0.0625	0.246603	0.6293	
SC	5.0625	1	5.0625	19.97486	0.0009	
FC	0.0625	1	0.0625	0.246603	0.6293	
P^2	185.0038	1	185.0038	729.9606	<0.0001	
G^2	223.6705	1	223.6705	882.5258	<0.0001	
S^2	223.6705	1	223.6705	882.5258	<0.0001	
F^2	91.00379	1	91.00379	359.0693	<0.0001	
C^2	266.0038	1	266.0038	1049.558	<0.0001	
Residual	2.787879	11	0.253444			
Lack of fit	1.287879	6	0.214646	0.715488	0.6558	Not significant
Pure error	1.5	5	0.3			
Corrected total	1306.719	31				
Std. Dev.	0.503432					
Mean	12.90625					
CV%	3.900682					
R^2	0.997867					
Adjusted R^2	0.993987					
Predicted R^2	0.971992					
Adequate precision	45.50177					

df: degrees of freedom; CV: coefficient of variation; *F*: Fisher ratio; *p*: probability

Table 4 ANOVA for the response porosity

Source	Sum of squares	df	Mean square	*F* value	*p* value Prob > *F*	
Model	1930.845	20	96.54223	350.4483	<0.0001	Significant
P, input power	400.1667	1	400.1667	1452.605	<0.0001	
G, primary gas flow rate	192.6667	1	192.6667	699.38	<0.0001	
S, stand-off distance	368.1667	1	368.1667	1336.445	<0.0001	
F, powder feed rate	112.6667	1	112.6667	408.98	<0.0001	
C, carrier gas flow rate	2.666667	1	2.666667	9.68	0.0099	
PG	6.25	1	6.25	22.6875	0.0006	
PS	16	1	16	58.08	<0.0001	
PF	1	1	1	3.63	0.0832	
PC	1	1	1	3.63	0.0832	
GS	1	1	1	3.63	0.0832	
GF	4	1	4	14.52	0.0029	
GC	4	1	4	14.52	0.0029	
SF	12.25	1	12.25	44.4675	<0.0001	
SC	0.25	1	0.25	0.9075	0.3612	
FC	30.25	1	30.25	109.8075	<0.0001	
P^2	173.4697	1	173.4697	629.695	<0.0001	
G^2	274.0947	1	274.0947	994.9638	<0.0001	
S^2	191.7614	1	191.7614	696.0938	<0.0001	
F^2	252.1364	1	252.1364	915.255	<0.0001	
C^2	139.6364	1	139.6364	506.88	<0.0001	
Residual	3.030303	11	0.275482			
Lack of fit	1.530303	6	0.255051	0.850168	0.5824	Not significant
Pure error	1.5	5	0.3			
Corrected total	1933.875	31				
Std. Dev.	0.524864					
Mean	14.4375					
CV%	3.635421					
R^2	0.998433					
Adjusted R^2	0.995584					
Predicted R^2	0.978937					
Adequate precision	50.56583					

df: degrees of freedom: CV: coefficient of variation; F: Fisher ratio; *p*: probability

representation which provides silhouette views of the response surface (Ref 31). The perturbation plot can be used to compare the effects of all factors at a particular point in the RSM design space. For response surface designs, the perturbation plot shows how the response changes as each factor moves from the chosen reference point, while all other factors remain constant at the reference value. Normally, Design-Expert software sets the reference point default at the middle of the design space (the coded zero level of each factor). A steep slope or curve in a factor shows that the response is sensitive in that factor. A relatively flat line shows insensitivity to change in that particular factor (Ref 32).

4.1 Effect of Input Power on Coating Properties

The effects of input power (curve A) on responses are displayed in the Fig. 5(a)-(e). From the figures, the following points can be inferred. Lower power levels gave improper melting of the particles, which resulted in poor quality coatings in terms of bond strength (Fig. 5b, c). As the arc current increases, the total and the net available energies in the plasma increase. This condition leads to a better in-flight particle molten state and higher velocities. The deposition yield reaches (Fig. 5a) a plateau for the highest current levels because of the increase in plasma jet temperature, which in turn increases both the particle melting ratio and the plasma jet viscosity for particles to flatten better. Increasing the power level increases the bond strength up to a certain extent. At an optimum power level, the melting of the particles is better, and after deposition, they form a stronger bonding with the substrate surface on solidification. A higher enthalpy in the plasma flame is likely to produce a larger fraction of molten particles and, generally, a higher deposition efficiency (Ref 33). Porosity decreases under high power levels (Fig. 5d) because the particles are more likely to melt at high plasma energy levels, thereby enhancing flow and compaction of the coating during its build up. If the velocity of the particles is increased and/or the viscosity is decreased, then particle spreading tends to increase.

The presence of non-molten particles will also increase the roughness of the coating and will lower the values of hardness because of low particle cohesion (Fig. 5e). This also should increase the porosity of the coatings. An increase in porosity will lower the coating stiffness, producing a decrease in the values of hardness. Under very high power levels, gas entrapment upon impact occurs because of the high pressure in the gas layer just prior to impact. During the rapid spreading and quenching of splats, gas escape can be suppressed resulting in escalating gas pressure in the splat center, which can create the thin

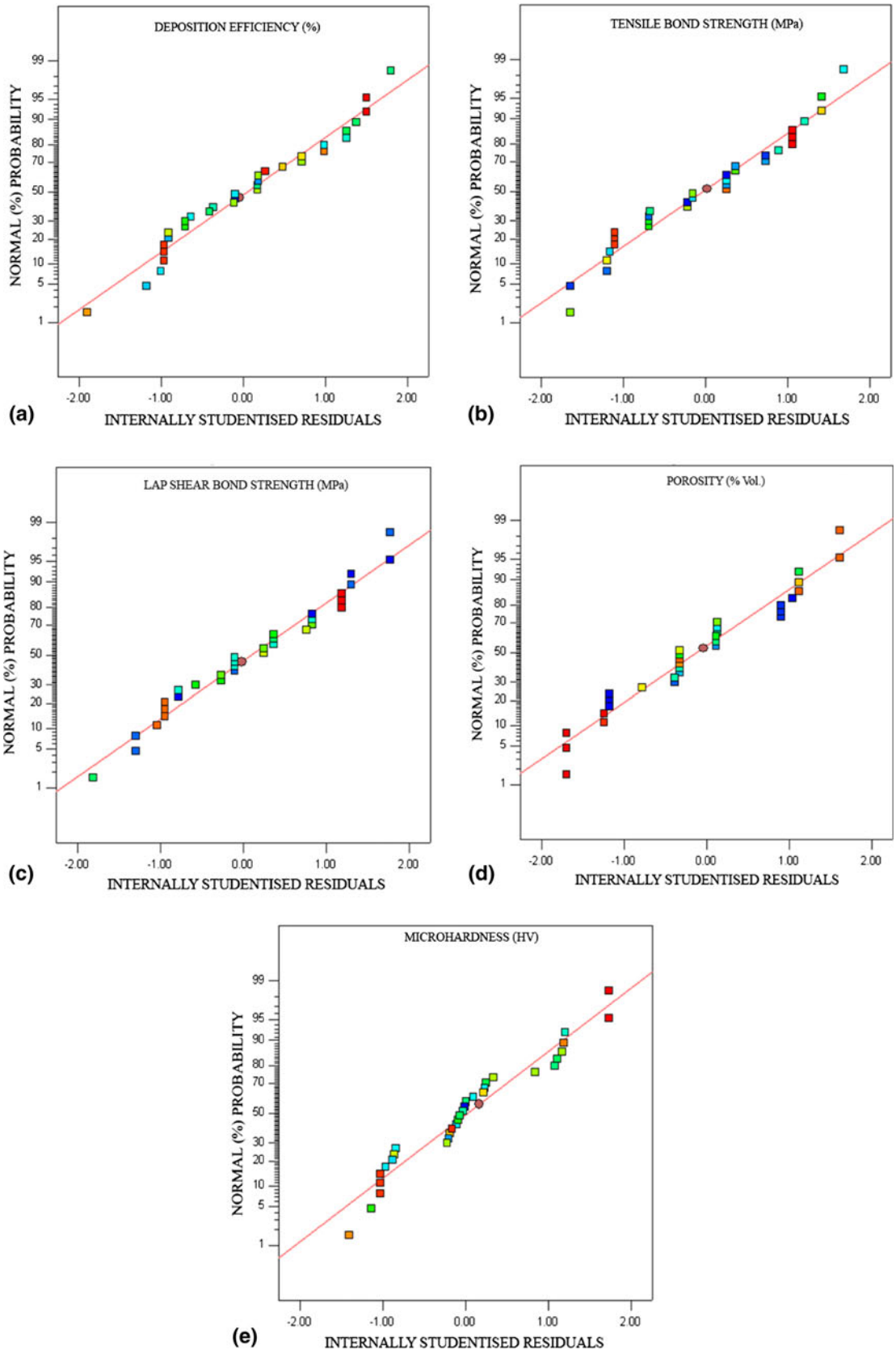

Fig. 3 Normal probability plots for the responses

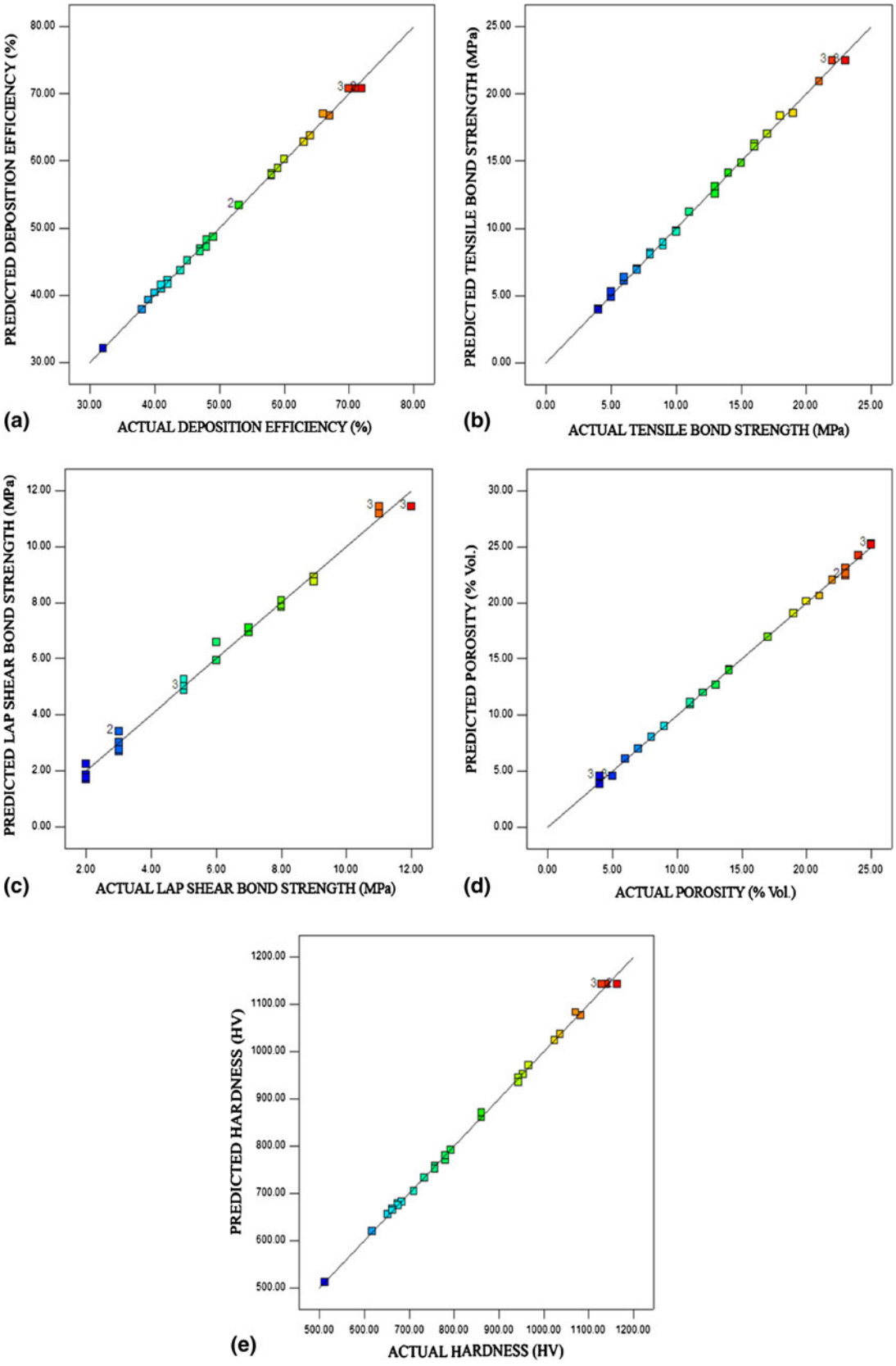

Fig. 4 Correlation plots for the responses

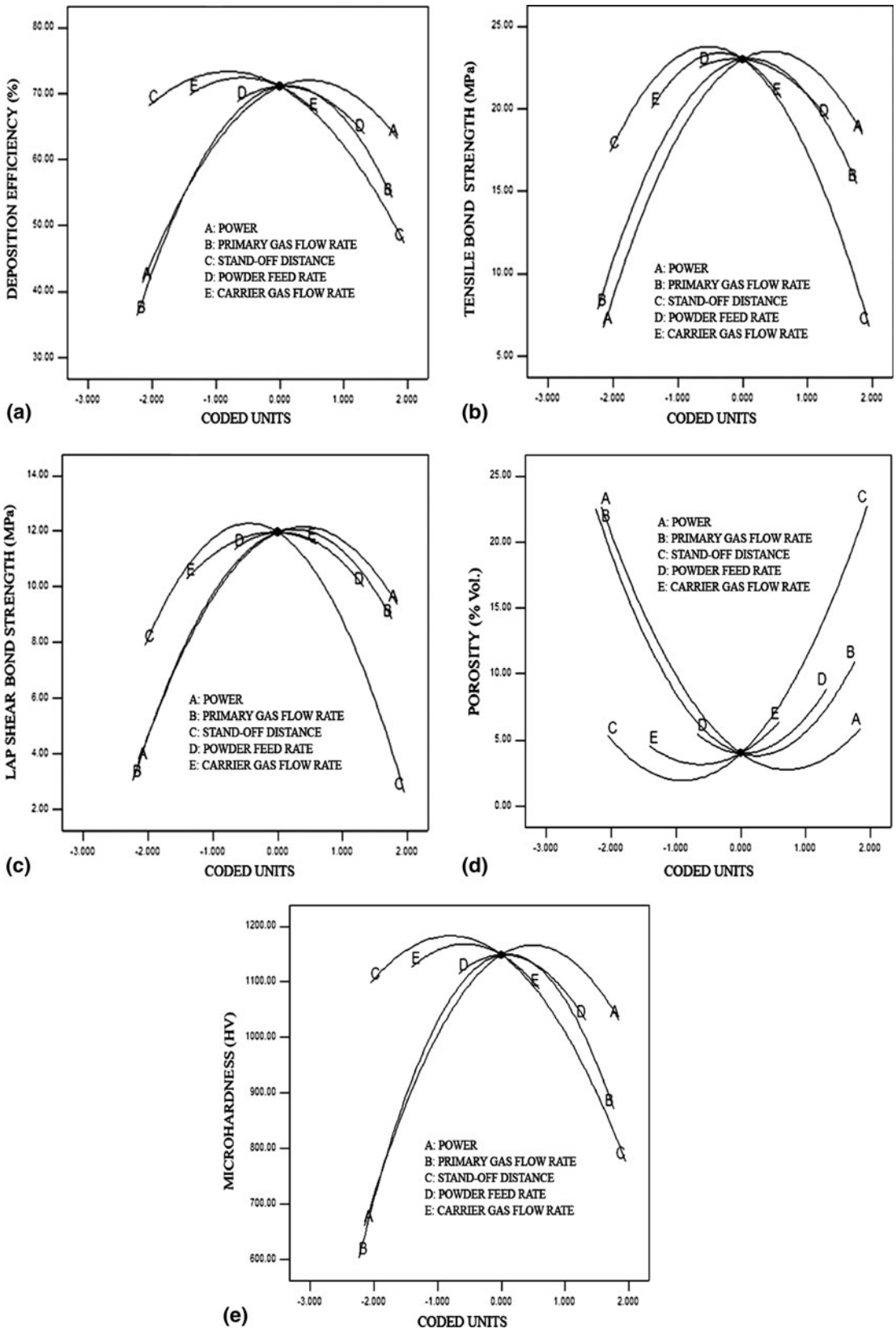

Fig. 5 Effect of process parameters on the responses (Perturbation plots)

cap of a gas bubble, leaving behind a residual hole causing an increase in porosity level and the reduction of hardness values (Ref 34). Very high power levels led to the decrease in deposition efficiency because of the vaporization of particles. Both the experimental and the predicted results agree in describing these effects.

4.2 Effect of Primary Gas Flow Rate on Coating Properties

The effects of primary gas flow rate (curve B) on responses are illustrated in the Fig. 5(a)-(e). If the primary gas flow rate is low, then it reduces the length of the plasma column, which in turn reduces the residential time of the particles in the plasma leading to poor melting and associated detrimental effects on the coating properties. Increasing argon flow will increase the particle velocity because the velocity of the plasma gas flame is proportional to the working gas mass flow rate. An increase in the gas flow rate above the optimal value increases the velocity but decreases the plasma jet temperature (Ref 35). Increasing the primary gas flow rate above a critical (optimal) value leads to a decrease in the largest particle melting state. Thus, only a few particles will succeed in plasma gas flow rate which leads to a decrease in the plasma/particle interaction duration ending up with a low deposition efficiency, a low hardness, a low bond strength, and high porosity.

The molecular ionization and the dissociation of the gas in the plasma jet are also affected under very high primary gas flow rates (Ref 36). Subsequently, conditions for spraying particles at an exact temperature and velocity may be obtained by carefully regulating both the power and the gas flow rates. The coatings sprayed under optimal primary gas flow (optimum velocity and enthalpy) condition shows high bond strength, hardness, and low porosity, compared with the low and high flow rate cases. Both the low and the high primary gas flow conditions lead to shorter flight times which minimize the plasma particle interactions.

4.3 Effect of Stand-Off Distance on Coating Properties

The variation of responses with stand-off distances (curve C) are displayed in the Fig. 5(a)-(e). It is seen that the bond strength increases with stand-off and attains a maximum, and then reduces. With smaller stand-off distance, the splashing of material with possible fragmentation and quenching cracks may result. This may promote porosity thereby reducing the bond strength (Ref 37). However, with higher-order stand-off distance, the reduction in the bond strength different attributes.

With longer stand-off distances, the enthalpy of the molten ceramic particles is largely lost, and the particles are decelerated in a relatively longer flight path because of the interaction with the surrounding air. Under such conditions, the particles striking on the substrate will not be adequately flattened to overlap the layers, resulting in porosity, and reduced bond strength and hardness values. In the case of optimum stand-off, the surface presents a fairly uniform texture, with striking material experiencing flattening without any cracking and showing excellent adhesion as observed in the bond strength tests. Optimum particle temperatures provide more effective packing of splats, and better cohesion between splats (Ref 38). The decrease in percentage porosity and increase in hardness, bond strength, and deposition efficiency is an indication of the effective packing and cohesion between splats.

4.4 Effect of Powder Feed Rate on Coating Properties

The effect of powder feed rate (curve D) on the responses of the coatings are displayed in the Fig. 5(a)-(e). Varying the powder feed rate affects the number of particles having to share the kinetic and thermal energies of the flame, which in turn affects the particle velocity and the temperature. Too low a powder feed rate will result in vaporization (decreases deposition efficiency), and over melting of the particles resulting in quench cracks (decreases hardness) (Ref 39, 40), splashing (decreases bond strength), and high porosity levels (decreases coating density), whereas too high a feed rate will end up in poor melting of the powder particles resulting in a decrease of the splat flattening ratio and an increase in the porosity (Ref 41).

However, the greater the number of particles in the flame is, the greater the deviation from the spraying axis will be, due both to a change in the powder inlet conditions and to an increase in the opportunities for particle collisions that change the trajectories of the colliding particles (Ref 42). A larger number of small and large particles will also float on top of the flame or penetrate it to reach the lower part. These particles not attaining sufficient velocity and temperature, however, either reach the coating or stick to it. Indeed, the in-flight processing of the powders to produce plasma-sprayed coatings must be performed under high loading conditions to allow for an efficient use of the thermal energy stored in the plasma (Ref 43). On exceeding a certain critical (optimal) loading, the particles interact with each other, and the momentum and temperature of the plasma jet will decrease with increasing mass of powder. Since the trajectories of the particles are very close to the axis of the jet, the plasma gas is significantly cooled down in that region. Higher feed rates will lead to even lower plasma temperatures (Ref 44).

4.5 Effect of Carrier Gas on Coating Properties

The effects of carrier gas flow rate (curve E) on the responses of the coatings are shown in the Fig. 5(a)-(e). The carrier gas flow rate is the rate at which the particles are injected into the plasma jet. Particles, in dc plasma spraying, should be injected with a momentum similar to that of the plasma jet (Ref 45). The flow rate must be sufficient to propel the particles from the feed canisters to the plasma. Optimally, the overwhelming part of the particles should be injected into the core of the plasma

stream so as to be carried along in the center of the jet to the substrate. Too high a carrier gas flow rates could result in particles' flight crossing through the jet axis resulting in a waste of powder. Influence of the nature of the carrier gas on the properties of the plasma jet rate to ensure sufficient particles penetration into the jet could lead to high jet perturbations.

In this study, argon was used as carrier gas. The injected carrier gas shifts the plasma jet into the opposite direction. Displacement of the jet is proportional to the carrier gas flow rate: the higher the carrier gas flow rate, the stronger the changes of the jet properties. However, even for very high flow rates, the position of the maximum carrier gas concentration is not congruent with the jet central line (Ref 46). It means that the injected particles are not penetrating the jet totally but are partially put aside. This could lead to improper particle heating and melting, decreasing the deposition efficiency of the spraying process due to wastage of powder. The deposition yield increases with an increase of the feedstock carrier gas flow rate, mostly because the particle injection velocity is increased—drifting the particles deeper into the jet core (i.e., optimal carrier gas flow rate leads to optimal radial position), thus improving their velocity and temperature resulting in high bond strength, hardness, and low porosity. However, when continuing to increase the gas flow rate, higher injection velocities are obtained until the particle ratio crossing the plasma jet becomes significant. This, in turn, decreases the deposition yield.

5. Process Optimization

To investigate the influencing tendency of the process parameters on the responses, 3D graphs were plotted under certain processing conditions. The 3D response surface and 2D contour plots are the graphical representations of the regression equations used to determine the optimum values of the variables within the ranges considered (Ref 31). Equation 10 (tensile bond strength) was used to plot the Fig. 6(a)-(d) (surface plots) and 7(a)-(d) (contour plots). Equation 12 (porosity) was used to plot the Fig. 6(e)-(h) (surface plots) and 7(e)-(h) (contour plots). It is clear from Fig. 6(a)-(d) that the tensile bond strength increases, reaches an apex, and then decreases with the increase in the levels of factors under consideration. The apex of the response plot shows the maximum tensile bond strength (the same trend was observed in the case of lap shear bond strength, deposition efficiency, and microhardness). From the Fig. 6(e)-(h), it is proposed that the porosity decreases, reaches a trough, and increases with the increase in the levels of considered process parameters. The valley (trough) of the response plot shows the minimum porosity. These response contours can help in the prediction of the responses for any zone of the experimental domain (Ref 47). The optimization module in design-expert searches for a combination of factor levels, which simultaneously satisfy the requirements placed (i.e., optimization criteria) on each of the responses and process factors (i.e., multiple response optimization) (Ref 48). Numerical and graphical optimization methods were used in this study by choosing the desired goals for each factor and response. The optimization process aims to combine the goals into an overall desirability function. The numerical optimization finds a point or more that maximize this function. However, in the graphical optimization with multiple responses, one has to define regions where requirements simultaneously meet the proposed criteria by superimposing or overlaying critical response contours on a contour plot. Then, visual search for the best compromise becomes possible.

In the case of dealing with many responses, it is recommended to perform numerical optimization first; otherwise, one may find it impossible to uncover a feasible region. The graphical optimization displays the area of feasible response values in the factor space. Regions that do not fit the optimization criteria are shaded (Ref 49). In the numerical optimization part, a criterion was adopted. The criterion is to maximize deposition efficiency, tensile bond strength, lap shear bond strength, and hardness, and to minimize porosity volume. In the case of graphical optimization for each response, the limits—lower and/or upper—have been chosen according to the numerical optimization results. The same criterion, which is proposed in the numerical optimization, was introduced in the graphical optimization. Contour plots play a very important role in the study of a response surface. The contour plots are illustrated in the Fig. 7(a)-(d) (tensile bond strength) and (e)-(h) (porosity). Each contour curve represents an infinite number of combinations of values of two test factors derived from the second-order quadratic equation within the considered range. The maximum predicted value is identified by the surface confined in the smallest ellipse or circle of the contour diagram. The circular contour plot indicates that the interactions between the corresponding factors are negligible, while the elliptical contour plot indicates that the interactions between the corresponding factors are significant (Ref 31).

Furthermore, a contour plot is produced to display the region of the optimal factor settings visually. For second-order response surfaces, such a plot can be more complex compared to the simple series of parallel lines that can occur with first-order empirical relationships. Once the stationary point is found, it is usually necessary to characterize the response surface in the immediate vicinity of the point. Characterization involves identifying whether the stationary point found is a minimum response or maximum response or a saddle point. To classify this, it is most straightforward to examine it through a contour plot (Ref 32).

By performing the numerical optimization, i.e., by solving Eq 9-13, analyzing the profile of the response surfaces and their corresponding contour plots (Fig. 7a-d, e-h), the response values are obtained (Table 5). The above mentioned response values could be achieved using the following optimized parameter settings: power—26.3 kW; stand-off distance—110.5 mm; primary gas flow rate—36.15 lpm; powder feed rate—23.35 gpm;

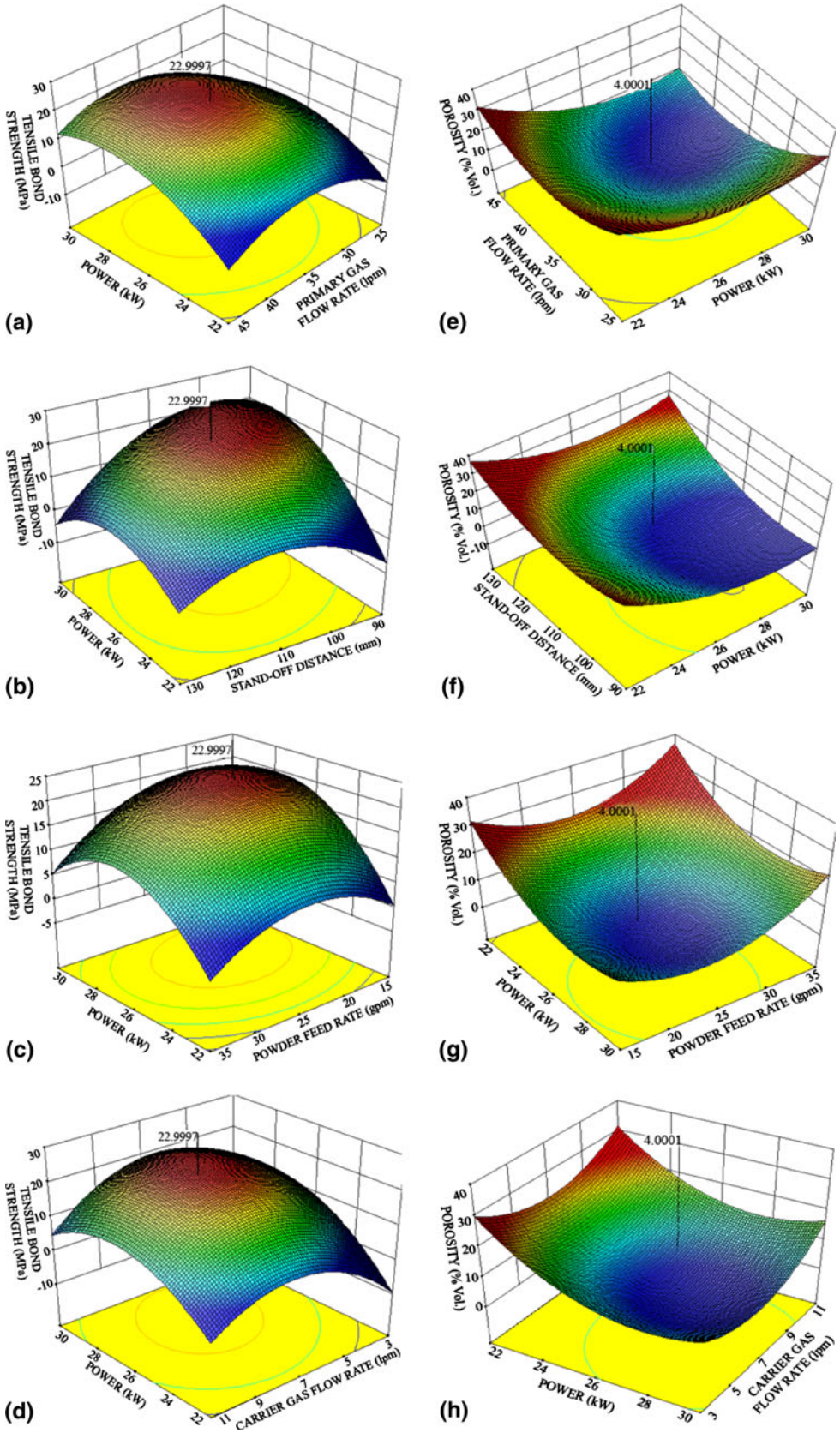

Fig. 6 Surface plots

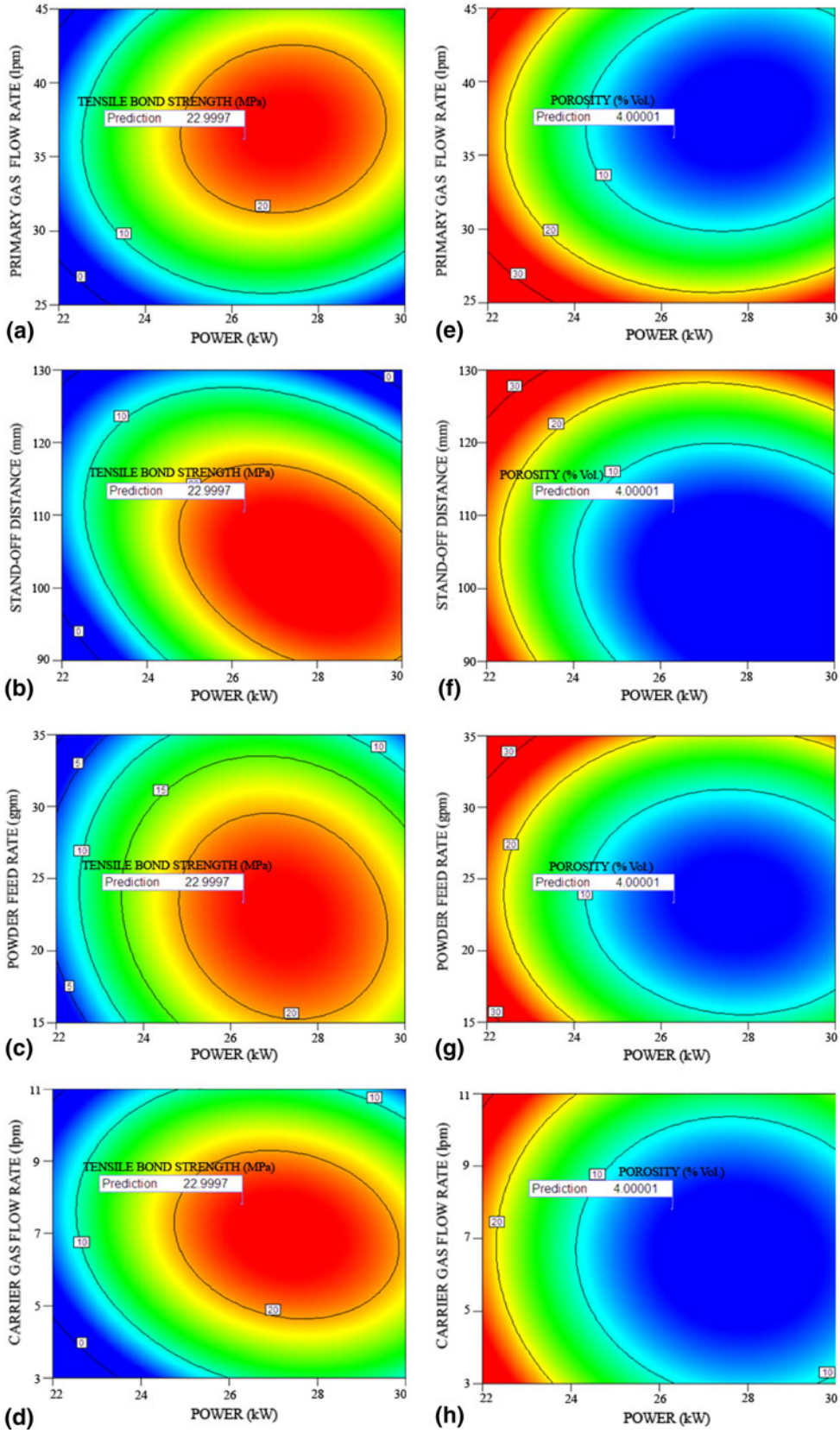

Fig. 7 Contour plots

Table 5 Results of responses achieved using optimized processing conditions

Responses	Numerical optimization	Graphical optimization	Validation
Deposition efficiency, %	71.0837	71.0825	72
Tensile bond strength, MPa	22.9997	22.9990	21
Lap shear bond strength, MPa	11.9612	11.9610	11
Porosity, vol.%	4.0001	4.0009	4
Hardness, HV 0.3	1148.94	1148.92	1153

and carrier gas flow rate—7.8 lpm. The above values (factor values and response values) were also verified using the graphical optimization. The graphical optimization result allows visual inspection to choose the optimum coating condition. The shaded areas on the overlay plot are the regions that do not meet the proposed criteria (Ref 49). The graphical optimization plot is displayed in Fig. 8. To validate the model, three additional confirmation experiments were conducted to compare the experimental results with the prediction under the optimal conditions. The mean experimental response results are tabulated in the Table 5. The validated response values show good agreement with the predicted values. The optical micrograph of the cross section of the coating produced under optimized processing condition is shown in Fig. 9. From Fig. 9 it could be inferred that, the microstructure of the coatings is strongly dependent on processing conditions. When an adequately molten particle hits the substrate, the sudden deceleration causes a pressure build-up at the particle-substrate interface; the high pressure inside the particle forces the melted material to flow laterally or the ductile solid material to deform. The liquid spreads outward from the point of impact and forms a splat. The arresting of spreading results from the conversion of the particle kinetic energy into the work of viscous deformation and surface energy (Ref 50). The process of splat

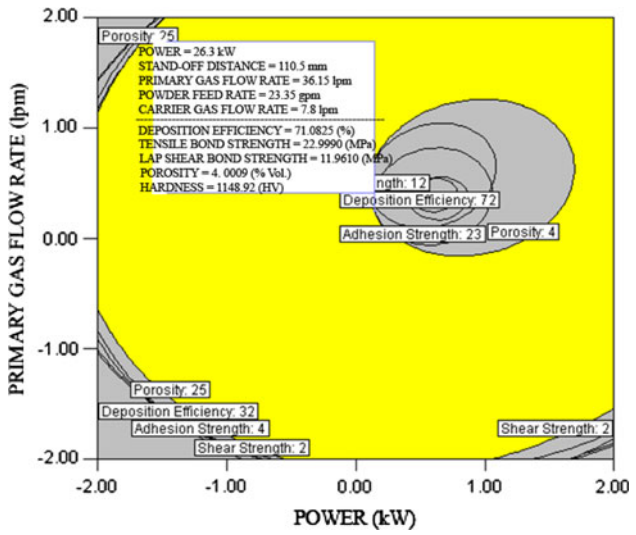

Fig. 8 Overlay plot

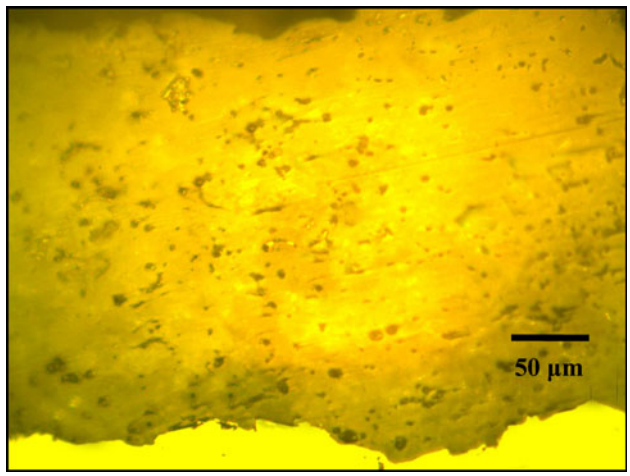

Fig. 9 Optical micrograph of the cross section of the coating produced under optimised processing condition

formation depends on the velocity, size, molten state, chemistry, and angle of impact of the droplets on the surface. It is also subject to the surface topography of the substrate, its temperature, and reactivity (Ref 51). This process determines both microstructural and macroscopic characteristics of the coating.

Optimum particle temperature corresponds to a decrease in the dynamic viscosity of the material, which together with optimum particle velocity, results in a higher degree of flattening. In addition, a higher degree of flattening corresponds to a decrease in splat thickness and a larger area of splat surface being in contact with the underlying material (Ref 52), which leads to a higher deposition efficiency, bond strength, microhardness, and low porosity. In the case of the coating produced under optimum spray conditions, owing to adequate in-flight temperature, most particles undergo melting, so that each splat covers more easily the surface topography onto which it flattens. The porosity of YSZ coatings sprayed under the optimum condition is the lowest attainable porosity level. Under non-optimal conditions, the volume fraction of porosity and the average size of pores were found to be high.

6. Conclusions

- The effects of atmospheric plasma spray parameters (power, stand-off distance, primary gas flow rate, powder feed rate, and carrier gas flow rate) on the porosity, deposition efficiency, hardness, lap shear bond strength, and tensile bond strength were investigated for YSZ coatings by adopting multiobjective optimization with RSM.
- These results were used to create empirical relationships to predict the optimum deposition conditions. The input power has the largest effect on the resultant coating properties. Process parameters such as stand-off distance, primary gas flow rate, powder feed

rate, and carrier gas flow rate each can be considered as the next most important parameters influencing the coating properties.

- The multi-response optimization with RSM successfully predicted the optimum deposition parameters which simultaneously minimized the porosity and increased the deposition efficiency, tensile bond strength, lap shear bond strength, and hardness.

Acknowledgments

The authors wish to express their sincere thanks to the Department of Science and Technology (DST), Govt. of India, New Delhi for the financial support extended to carry out this investigation through the sponsored fast-track scheme for young scientists—R&D project No. SR/FT/ETA-01/2009. The help provided by Mr. A. K. Lakshminarayanan (PhD Scholar, the Dept. of Manufacturing Engg., Annamalai University) in the statistical part of this article is greatly acknowledged.

References

1. T. Beck, R. Herzog, O. Trunova, M. Offermann, R.W. Steinbrech, and L. Singheiser, Damage Mechanisms and Lifetime Behavior of Plasma-Sprayed Thermal Barrier Coating Systems for Gas Turbines. Part II. Modeling, *Surf. Coat. Technol.*, 2008, **202**, p 5901-5908
2. J. Gómez-García, A. Rico, M.A. Garrido-Maneiro, C.J. Múnez, P. Poza, and V. Utrilla, Correlation of Mechanical Properties and Electrochemical Impedance Spectroscopy Analysis of Thermal Barrier Coatings, *Surf. Coat. Technol.*, 2009, **204**, p 812-815
3. S.-I. Jung, J.-H. Kim, J.-H. Lee, Y.-G. Jung, U. Paik, and K.-S. Lee, Microstructure and Mechanical Properties of Zirconia-Based Thermal Barrier Coatings with Starting Powder Morphology, *Surf. Coat. Technol.*, 2009, **204**, p 802-806
4. S.A. Sadeghi-Fadaki, K. Zangeneh-Madar, and Z. Valefi, The Adhesion Strength and Indentation Toughness of Plasma-Sprayed Yttria Stabilized Zirconia Coatings, *Surf. Coat. Technol.*, 2010, **204**, p 2136-2141
5. P. Diez and R.W. Smith, The Influence of Powder Agglomeration Methods on Plasma Sprayed Yttria Coatings, *J. Therm. Spray Technol.*, 1993, **2**, p 165-172
6. A. Kulkarni, A. Vaidya, A. Goland, S. Sampath, and H. Herman, Processing Effects on Porosity-Property Correlations in Plasma Sprayed Yttria-Stabilized Zirconia Coatings, *Mater. Sci. Eng. A*, 2003, **359**, p 100-111
7. R. Kingswell, K.T. Scott, and L.L. Wassell, Optimizing the Vacuum Plasma Spray Deposition of Metal, Ceramic and Cermet Coatings Using Designed Experiments, *J. Therm. Spray Technol.*, 1993, **2**, p 179-186
8. Y. Wang and T.W. Coyle, Optimization of Solution Precursor Plasma Spray Process by Statistical Design of Experiment, *J. Therm. Spray Technol.*, 2008, **17**, p 692-699
9. Troczynski and M. Plamondon, Response Surface Methodology for Optimization of Plasma Spraying, *J. Therm. Spray Technol.*, 1992, **1**, p 293-300
10. F.H. Yuan, Z.X. Chen, Z.W. Huang, Z.G. Wang, and S.J. Zhu, Oxidation Behavior of Thermal Barrier Coatings with HVOF and Detonation-Sprayed NiCrAlY Bondcoats, *Corros. Sci.*, 2008, **50**, p 1608-1617
11. E. Lugscheider, F. Ladru, V. Gourlaouen, and C. Gualco, Enhanced Atmospheric Plasma Spraying of Thick TBCs by Improved Process Control and Deposition Efficiency, *Thermal Spray: Meeting the Challenges of the 21st Century*, C. Coddet, Ed., May 25-29, 1998 (Nice, France), ASM International, 1998, 1693 p
12. J. Wigren and L. Pejryd, Thermal Barrier Coatings-Why, How, Where and Where to, *Thermal Spray: Meeting the Challenges of the 21st Century*, C. Coddet, Ed., May 25-29, 1998 (Nice, France), ASM International, 1998, 1693 p
13. K.C. Chang, W.J. Wei, and C. Chen, Oxidation Behavior of Thermal Barrier Coatings Modified by Laser Remelting, *Surf. Coat. Technol.*, 1998, **102**, p 197-204
14. P.-C. Tsai, J.-H. Lee, and C.-L. Chang, Improving the Erosion Resistance of Plasma-Sprayed Zirconia Thermal Barrier Coatings by Laser Glazing, *Surf. Coat. Technol.*, 2007, **202**, p 719-724
15. M. Prystay, P. Gougeon, and C. Moreau, Structure of Plasma-Sprayed Zirconia Coatings Tailored by Controlling the Temperature and Velocity of the Sprayed Particles, *J. Therm. Spray Technol.*, 2001, **10**, p 67-75
16. M. Friis, C. Persson, and J. Wigren, Influence of Particle In-Flight Characteristic on the Microstructure of Atmospheric Plasma Sprayed Yttria Stabilized ZrO_2, *Surf. Coat. Technol.*, 2001, **141**, p 115-127
17. A. Kucuk, R.S. Lima, and C.C. Berndt, Influence of Plasma Spray Parameters on In-Flight Characteristics of ZrO_2-8(wt.%)Y_2O_3 Ceramic Particles, *J. Am. Ceram. Soc.*, 2001, **84**, p 685-692
18. A. Kucuk, R.S. Lima, and C.C. Berndt, Influence of Plasma Spray Parameters on Formation and Morphology of ZrO_2-8(wt.%)Y_2O_3 Ceramic Particles, *J. Am. Ceram. Soc.*, 2001, **84**, p 693-700
19. R. Suryanarayanan, *Plasma Spraying: Theory and Applications*, World Scientific Publishing, New York, 1993
20. R.B. Hiemann, *Plasma-Spray Coating-Principles and Applications*, Wiley VCH Publishers Inc., New York, 1996
21. L. Pawlowski, *The Science Engineering of Thermal Spray Coatings*, 2nd ed., John Wiley & Sons Ltd, London, 2008
22. A.I. Khuri and J.A. Cornell, *Response Surfaces; Design and Analysis*, Marcel Dekker Ltd, New York, 1996
23. R.G. Miller, J.E. Freund, and D.E. Johnson, *Probability and Statistics for Engineers*, Prentice of Hall of India Pvt Ltd., New Delhi, 1999
24. D.C. Montgomery, *Design and Analysis of Experiments*, John Wiley & Sons Ltd, New Delhi, 2007
25. C.R.C. Lima and J.M. Guilemany, Adhesion Improvements of Thermal Barrier Coatings with HVOF Thermally Sprayed Bond Coats, *Surf. Coat. Technol.*, 2007, **201**, p 4694-4701
26. K.Y. Benyounis and A.G. Olabi, Optimization of Different Welding Processes Using Statistical and Numerical Approaches—A Reference Guide, *Adv. Eng. Softw.*, 2008, **39**, p 483-496
27. A.R. Hamad, J.H. Abboud, F.M. Shuaeib, and K.Y. Benyounis, Surface Hardening of Commercially Pure Titanium by Laser Nitriding: Response Surface Analysis, *Adv. Eng. Softw.*, 2010, **41**, p 674-679
28. H. Öktem, T. Erzurumlu, and H. Kurtaran, Application of Response Surface Methodology in the Optimization of Cutting Conditions for Surface Roughness, *J. Mater. Process. Technol.*, 2005, **170**, p 11-16
29. A.S. Shahi and S. Pandey, Modelling of the Effects of Welding Conditions on Dilution of Stainless Steel Claddings Produced by Gas Metal Arc Welding Procedures, *J. Mater. Process. Technol.*, 2008, **196**, p 339-344
30. S. Kumar, P. Kumar, and H.S. Shan, Effect of Evaporative Pattern Casting Process Parameters on the Surface Roughness of Al-7% Si Alloy Castings, *J. Mater. Process. Technol.*, 2007, **182**, p 615-623
31. G.E.P. Box and N.R. Draper, *Empirical Model-Building and Response Surfaces*, John Wiley & Sons, Inc., New York, 1986
32. R.H. Myers and D.C. Montgomery, *Response Surface Methodology*, John Wiley & Sons, Inc., New York, 2002
33. J.F. Li, H. Liao, B. Normand, C. Cordier, G. Maurin, J. Foct, and C. Coddet, Uniform Design Method for Optimization of Process Parameters of Plasma Sprayed TiN Coatings, *Surf. Coat. Technol.*, 2003, **176**, p 1-13
34. G. Montavon, C.C. Berndt, C. Coddet, S. Sampath, and H. Herman, Quality Control of the Intrinsic Deposition Efficiency from the Controls of the Splat Morphologies and the Deposit Microstructure, *J. Therm. Spray Technol.*, 1997, **6**, p 153-166

35. H.D. Steffens and T. Duda, Enthalpy Measurements of Direct Current Plasma Jets Used for ZrO_2 $7Y_2O_3$ Thermal Barrier Coatings, *J. Therm. Spray Technol.*, 2000, **9**, p 235-240
36. T. Streibl, A. Vaidya, M. Friis, V. Srinivasan, and S. Sampath, A Critical Assessment of Particle Temperature Distributions During Plasma Spraying: Experimental Results for YSZ, *Plasma. Chem. Plasma Process.*, 2006, **26**, p 73-102
37. A. Kucuk, C.C. Berndt, U. Senturk, R.S. Lima, and C.R.C. Lima, Influence of Plasma Spray Parameters on Mechanical Properties of Yttria Stabilized Zirconia Coatings. I. Four Point Bend Test, *Mater. Sci. Eng. A*, 2000, **284**, p 29-40
38. S. Guessasma, Z. Salhi, G. Montavon, P. Gougeon, and C. Coddet, Artificial Intelligence Implementation in the APS Process Diagnostic, *Mater. Sci. Eng. B*, 2004, **110**, p 285-295
39. S. Kuroda, T. Fukushima, and S. Kitahara, Significance of Quenching Stress in the Cohesion and Adhesion of Thermally Sprayed Coatings, *J. Therm. Spray Technol.*, 1992, **1**, p 325-332
40. S. Kuroda, T. Dendo, and S. Kitahara, Quenching Stress in Plasma Sprayed Coatings and Its Correlation with the Deposit Microstructure, *J. Therm. Spray Technol.*, 1995, **4**, p 75-84
41. Y. Liu, T. Nakamura, V. Srinivasan, A. Vaidya, A. Gouldstone, and S. Sampath, Non-Linear Elastic Properties of Plasma-Sprayed Zirconia Coatings and Associated Relationships with Processing Conditions, *Acta Mater.*, 2007, **55**, p 4667-4678
42. M. Vardelle, A. Vardelle, P. Fauchais, K.I. Li, B. Dussoubs, and N.J. Themelis, Controlling Particle Injection in Plasma Spraying, *J. Therm. Spray Technol.*, 2001, **10**, p 267-284
43. P. Fauchais, Understanding Plasma Spraying, *J. Phys. D Appl. Phys.*, 2004, **37**, p 86-108
44. R.L. Williamson, J.R. Fincke, and C.H. Chang, A Computational Examination of the Sources of Statistical Variance in Particle Parameters During Thermal Plasma Spraying, *Plasma. Chem. Plasma Process.*, 2000, **20**, p 299-324
45. T. Kavka and A. Maslani, Influence of Injection Mode on Properties of DC Plasma Jets for Thermal Plasma Spraying, *Czech. J. Phys.*, 2004, **54**, p 766-771
46. R.L. Williamson, J.R. Fincke, and C.H. Chang, Numerical Study of the Relative Importance of Turbulence, Particle Size and Density and Injection Parameters on Particle Behavior During Thermal Plasma Spraying, *J. Therm. Spray Technol.*, 2002, **11**, p 107-118
47. A.K. Lakshminarayanan, V. Balasubramanian, R. Varahamoorthy, and S. Babu, Predicting the Dilution of Plasma Transferred Arc Hardfacing of Stellite on Carbon Steel using Response Surface Methodology, *Met. Mater. Int.*, 2008, **14**, p 779-789
48. K.Y. Benyounis, A.G. Olabi, and M.S.J. Hashmi, Optimizing the Laser-Welded Butt Joints of Medium Carbon Steel Using RSM, *J. Mater. Process. Technol.*, 2005, **164**, p 986-989
49. Design-Expert Software, *V8 User's Guide, Technical Manual*, Stat Ease, Inc., Minneapolis, 2008
50. R. Soltani, T.W. Coyle, J. Mostaghimi, R.S. Lima, and C. Moreau, Thermo-Physical Properties of Plasma Sprayed Yttria Stabilized Zirconia Coatings, *Surf. Coat. Technol.*, 2008, **202**, p 3954-3959
51. G. Bertrand, P. Bertrand, P. Roy, C. Rio, and R. Mevrel, Low Conductivity Plasma Sprayed Thermal Barrier Coating Using Hollow PSZ Spheres: Correlation Between Thermophysical Properties and Microstructure, *Surf. Coat. Technol.*, 2008, **202**, p 1994-2001
52. H. Guo, S. Kuroda, and H. Murakami, Microstructures and Properties of Plasma-Sprayed Segmented Thermal Barrier Coatings, *J. Am. Ceram. Soc.*, 2006, **89**, p 1432-1439